The effect of flow-derived mechanical cues on the growth and morphology of platelet aggregates under low, medium, and high shear rates

Hao, Y.; Tersteeg, C.; Hoekstra, A.G.; Závodszky, G.

DOI
10.1016/j.compbiomed.2024.109010

Publication date
2024

Document Version
Final published version

Published in
Computers in Biology and Medicine

Computers in Biology and Medicine 180 (2024) 109010

Contents lists available at ScienceDirect

Computers in Biology and Medicine

journal homepage: www.elsevier.com/locate/compbiomed

The effect of flow-derived mechanical cues on the growth and morphology of platelet aggregates under low, medium, and high shear rates

Yue Hao [a], Claudia Tersteeg [b], Alfons G. Hoekstra [a], Gábor Závodszky [a,c,*]

[a] Computational Science Lab, Informatics Institute, University of Amsterdam, Amsterdam, The Netherlands
[b] Laboratory for Thrombosis Research, IRF Life Sciences, KU Leuven Campus Kulak Kortrijk, Kortrijk, Belgium
[c] Department of Hydrodynamic Systems, Budapest University of Technology and Economics, Budapest, Hungary

ARTICLE INFO

Keywords:
Platelet aggregation
Confocal microscopy
Biomechanical pathways
von Willebrand Factor
Binding availability time
Shear rate gradient

ABSTRACT

Platelet aggregation is a dynamic process that can obstruct blood flow, leading to cardiovascular diseases. While many studies have demonstrated clear connections between shear rate and platelet aggregation, the impact of flow-derived mechanical signals on this process is not fully understood. The objective of this work is to investigate the role of flow conditions on platelet aggregation dynamics, including effects on growth, shape, density composition, and their potential correlation with binding processes that are characterised by longer (e.g., via αIIbβ3 integrin) and shorter (e.g., via VWF) initial binding times. *In vitro* blood perfusion experiments were conducted at wall shear rates of 800, 1600 and 4000 s^{-1}. Detailed analysis of two modalities of experimental images was performed to offer insights into the morphology of platelet aggregates. A consistent structural pattern was observed across all samples: a high-density core enveloped by a low-density outer shell. An image-based 3D computational blood flow model was subsequently employed to study the local flow conditions, including binding availability time and flow-derived mechanical signals via shear rate and rate of elongation. The results show substantial dependence of the aggregation dynamics on these flow parameters. We found that the different binding mechanisms that prefer different flow regimes do not have a monotonic cross-over in efficiency as the flow increases. There is a significant dip in the cumulative aggregation potential in-between the preferred regimes. The results suggest that treatments targeting the biomechanical pathways could benefit from creating conditions that exploit these low-efficiency zones of aggregation.

1. Introduction

Cardiovascular diseases are the leading cause of morbidity and mortality worldwide [1]. As a significant complication of cardiovascular disease, thrombosis can account for myocardial infarction, acute ischemic stroke, and venous thromboembolism [2,3]. To control pathological thrombus formation (that often initiates with the rapid aggregation of platelets), numerous drugs such as blood thinners have been developed and applied clinically [4,5]. These drugs target the soluble agonist-dependent (biochemical) axis of platelet aggregation to inhibit the pathological platelet response. However, the effects can interfere with the physiological hemostatic responses as well [6]. This can result in bleeding issues with serious consequences for patients [7]. Recent studies have highlighted the significance of fluid mechanical features, which primarily drive early platelet aggregation and platelet adhesion in thrombosis [8–10]. Under low shear regimes, the aggregation is dominated by α IIbβ3-dependent interactions, while with the increase of the flow rate, von Willebrand factor (VWF) contributes gradually more to the aggregation [11,12]. By understanding the fluid mechanical properties in the micro-environment of the platelet aggregates during the formation, we can identify the role of biomechanical pathways at the initial stage of thrombus formation.

Under low shear rate flow conditions, platelet activation triggers a significant conformational change in the integrin α IIbβ3 (also known as GPIIb/IIIa) via inside-out and then outside-in signalling pathways [13]. This conformational alteration allows α IIbβ3 to bind fibrinogen, initiating a pivotal receptor–ligand interaction that culminates in a platelet plug [14]. The α IIbβ3-fibrinogen-α IIbβ3 bond formed during this interaction is strong and long-lived, featuring remarkably low disengagement rates [11,15]. However, this strong bond requires more time for its initiation. Litvinov et al. [16] reported that the contact time required to reach half-maximal fibrinogen binding is 1 ms in the case of a relatively weak bond with rupture force around 20–40 pN. For more stable bonds, the required contact time is further extended: 20 ms for

* Corresponding author.
E-mail address: g.zavodszky@uva.nl (G. Závodszky).

https://doi.org/10.1016/j.compbiomed.2024.109010
Received 21 June 2024; Received in revised form 4 August 2024; Accepted 7 August 2024
Available online 18 August 2024

bonds featuring rupture forces of 40–60 pN, and 70 ms for the 60 pN force regimes.

Under high shear rate regimes, ensuring such a long binding time becomes challenging. Instead, an additional mechanosensitive binding process activates which can capture fast-moving platelets from the flow via VWF [17,18]. VWF, a large multimeric protein, functions as a bridging molecule between platelets and the injured vessel site to mediate platelet adhesion and aggregation under certain hydrodynamic forces [12]. VWF remains "coiled" or in a globular conformation under low shear forces, in which the binding sites in the A1 domain are inaccessible to platelet receptors [19,20]. When the shear rate or the rate of elongational reaches a threshold, the VWF undergoes conformation changes, including periodic elongation, thereby exposing the A1 epitopes [21]. The trigger threshold of the shear rate that unfolds VWF has been reported between 5000 and 5522 s^{-1} in pure-shear free flow [22,23], while in physiological flows, this threshold can decrease to approximately 2000–3000 s^{-1} [24,25]. Moreover, according to [24], elongational rates (as opposed to shear rates) need only to exceed 600 s^{-1} for the compact conformation of VWF to change.

Although the associated mechanisms that lead to hemostasis and thrombosis are fundamentally complex, the resulting thrombus structures follow certain patterns [26]. During thrombus formation, a "core" with highly activated, densely packed platelets is formed close to the injury site, and covered by a "shell" composed of less dense platelets [27]. The different platelet density of core and shell leads to different porosity and the amount of fluid permeating these regions [28]. Stalker et al. [27] and Welsh et al. [29] have reported porosity distribution inside a clot through *in vivo* experiments. However, both of their investigations are confined to 2-dimensional projection. Furthermore, to understand the influence of clot structure on blood flow, the permeability has been evaluated using several experimental techniques in [30,31]. The findings on permeability, however, are often subject to unique conditions that makes generalisation to other contexts challenging due to considerable variations in the experimental setup, flow composition and formation heterogeneity of thrombus. In case of available porosity information, a widely adopted solution for either platelet aggregates or full clots is to apply the Kozeny–Carman formula, which approximates the permeability based on the volume fraction and geometric characteristics of the solid components that comprise the porous material [32,33].

It is well-established that the governing flow conditions (e.g., high or low shear) have a significant impact on the platelet aggregation mechanism [34–37]. While thrombus formation and platelet adhesion models have been developed to investigate the platelet aggregation process incorporating the effect of local fluid mechanical cues [38–40], significant differences still exist between the morphology of a real aggregate and the one formed by computational models. Furthermore, gradients of shear also have a strong influence [15,24], however, such gradients can show strong heterogeneity around the aggregates [41]. Due to current technological limitations it is difficult to measure these flow conditions with sufficient detail. In this work we probe the connection between the morphologies of developing platelet aggregates and the surrounding flow micro-environment by complementing *in vitro* measurements with *in silico* techniques. We combine a series of microfluidic essays with high-resolution computational models of each aggregate to extract detailed information on the conditions of the aggregation process under low, medium, and high shear rate settings. The computed flow properties are mapped to variations in preferred growth direction and density distribution across all 84 aggregate samples. The aggregates have been recorded at multiple times during their growth to affirm the causal effect of the local flow conditions on these morphological variations.

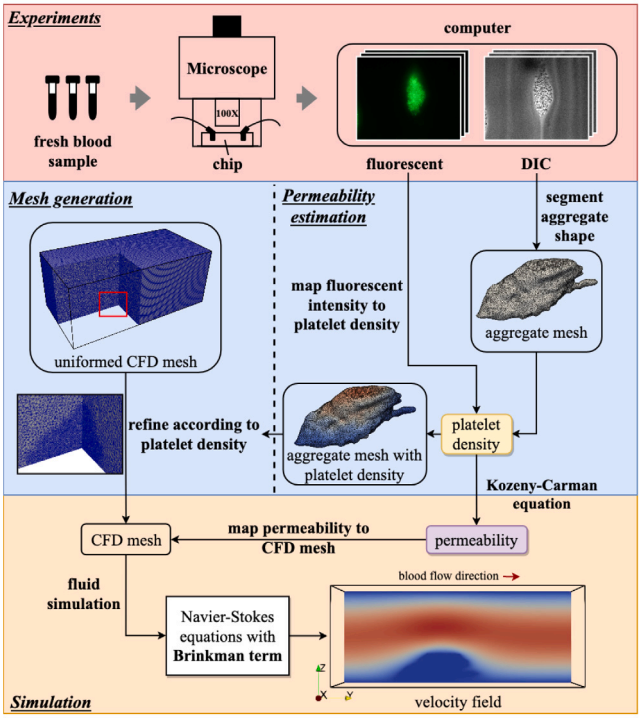

Fig. 1. Flow diagram for the image-based modelling methodology implemented in this work. The red block (at the top) represents the experimental process, in which the microscopy images of platelet aggregates with labelled and non-labelled platelets were imaged by DIC and fluorescent microscopy with 100x magnification. The blue block (at the middle) represents the data processing algorithm, including mesh generation and permeability estimation. The yellow block (at the bottom) represents the blood flow simulation part. The dimension of the simulation domain is 125 μm × 250 μm × 100 μm.

2. Methodology

2.1. Experiments and image processing

The overall schematic workflow of the approach employed in this work is summarised in Fig. 1. All the experiments were performed at the Laboratory for Thrombosis Research at KU Leuven, as described in [41]. Briefly, platelet aggregation was induced with citrated fresh human blood on μ-Slide VI 0.1 chips (Ibidi, Germany) in a chamber of 1 mm width and 100 μm height. The complete surface of the chamber was coated with 100 μg/mL Horm-collagen (Takeda, Austria), and the aggregates were visualised via an Axio Observer Z1 inverted fluorescence microscope (Zeiss, Germany) using differential interference contrast (DIC) and fluorescence microscopy at 100x magnification. Blood was mixed for 10 min at 37 °C with 2 μM DioC6 (Invitrogen) to label the platelets. The blood perfusion velocity was specified to 800, 1600 and 4000 s^{-1} wall shear rates (WSRs). The images were captured at 1, 2, 4, 6, 9 and 12 min after blood perfusion with a dimension of 125 μm × 100 μm × 100 μm. Two modalities of images were collected: DIC images to capture the shape of the outlines of platelet aggregates, and fluorescent images which employed labelling platelets to infers the internal density.

The DIC images were segmented using 3D Slicer [42] to obtain the outline of the platelet aggregates. Along with the fluorescent images, the platelet density within the aggregates was estimated. A manual platelet counting method was applied, and the relation between fluorescence intensity and platelet density of the entire aggregates was inferred via linear regression. Details of the procedure can be found in [41]. Subsequently, the Kozeny–Carman relation was employed to estimate the permeability. Next, a uniform computational fluid dy-

Table 1
Parameters used in simulations.

	Description	Value	Unit
ρ	Density of fluid	1.025×10^{-3} [45]	g mm^{-3}
μ	Fluid viscosity	3×10^{-3} [26,46]	g mm^{-1} s^{-1}
Φ_s	Sphericity of platelet	0.71 [47]	–
D_p	Platelet diameter	2×10^{-3} [48]	mm
dt	Time-step size	10^{-5}	s

namic (CFD) mesh was generated in Gmsh [43], which was subsequently refined to element size between 1 μm to 2.5 μm based on the local platelet density. This refinement increases the numerical accuracy in the vicinity of the aggregate, while reducing computational cost in the bulk of the flow.

Once the experimental images were processed, the permeability of platelet aggregates was interpolated to the CFD mesh. This procedure facilitates the precise assignment of permeability values from the aggregates to a specific location in the simulated domain, which is necessary to accurately capture the effect of the platelet aggregate on the blood flow in the simulation. Finally, the finite element method was applied to resolve the blood flow simulation based on the Navier–Stokes equations.

2.2. Computational blood flow model

In our simulations, the platelet aggregates were modelled as a porous medium, with their porosity directly associated with platelet density. The blood flow was modelled as an incompressible Newtonian fluid using the Navier–Stokes equations:

$$\rho\left(\frac{\partial \mathbf{u}}{\partial t} + \mathbf{u}\cdot\nabla\mathbf{u}\right) = -\nabla p + \mu\Delta\mathbf{u} - \frac{\mu}{k}\mathbf{u}, \qquad \nabla\cdot\mathbf{u} = 0, \tag{1}$$

where $\mathbf{u}$, p, ρ and μ are the flow velocity, pressure, blood density and blood viscosity, respectively. The impact of the platelet aggregates on the flow field was incorporated into the last term (Brinkman term) on the right-hand side of the equation according to Darcy's law. In this term, k is the permeability of the platelet aggregates, which was estimated using the Kozeny–Carman equation,

$$k = \Phi_s^2 \frac{\epsilon^3 D_p^2}{150\,(1-\epsilon)^2}. \tag{2}$$

Here, Φ_s is the sphericity of the platelets, ϵ is the porosity of the aggregates and D_p represents the platelet diameter.

The parameter values used in the model and their literature sources are listed in Table 1. The time-step size was chosen to satisfy the Courant–Friedrichs–Lewy condition [44]. In the simulation, the blood flowed into the domain along the y direction, as shown in the velocity field snapshot in Fig. 1. At the inlet, a constant velocity profile was prescribed in the x direction, given that the blood flow domain was considered as a small part of the channel in the x direction, while a parabolic velocity profile was specified in the z direction. At the outlet, a constant pressure condition was used. No-slip boundary conditions were imposed at the top and bottom walls and periodic boundaries in the y direction.

The simulation was implemented with FreeFEM [49] and simulations were executed on the Dutch national supercomputer Snelllius (SURF, The Netherlands) on 128 AMD Rome 7H12 CPU×2 cores. The corresponding source codes are available at: https://github.com/yhao9s9/aggregation-dynamics-investigation.

2.3. Local binding availability time

The low shear rate binding interaction between α IIbβ3 and fibrinogen requires a longer time to form the bond. The estimation of this local binding availability time at location $\mathbf{x}$ was approximated as follows:

$$T_{\text{avail}}(\mathbf{x}) = \frac{1}{|\mathbf{u}(\mathbf{x})|} \times L, \tag{3}$$

where $|\mathbf{u}(\mathbf{x})|$ denotes the velocity magnitude of blood flow at position $\mathbf{x}$, and L denotes the binding distance of fibrinogen, which is 45 nm [50].

2.4. Fluid mechanical properties

The high shear rate binding process, involving the interaction between VWF binding to GPIbα, is notably affected by the mechanosensitivity of VWF. It is strongly correlated to both the rate of elongation and shear rate. Hence, the shear rate and the rate of elongation were also calculated.

Here, the shear rate magnitude $\dot{\gamma}$ was obtained by:

$$\dot{\gamma} = \sqrt{2 \times D : D}, \tag{4}$$

where D represents the strain rate tensor which is defined as $D = \frac{1}{2}(\nabla\mathbf{u} + \nabla\mathbf{u}^T)$. Furthermore, the rate of the uni-axial elongation is defined as the magnitude of the diagonal elements of the rate of the flow strain tensor [51–53]:

$$\dot{\epsilon} = \sqrt{\left(\frac{\partial u}{\partial x}\right)^2 + \left(\frac{\partial v}{\partial y}\right)^2 + \left(\frac{\partial w}{\partial z}\right)^2}, \tag{5}$$

where $[u, v, w]^{\mathrm{T}} = \mathbf{u}$ are the velocity components in each direction.

3. Results

The results were collected at multiple time-points during the flow exposure period and evaluated in three steps. First, we focused on the aggregate morphology in terms of shape and dimensions. Second, the internal platelet density distribution was evaluated using the combination of the two employed imaging modalities. This density is directly related to porosity (ϵ) as $1 - \epsilon$, from which permeability was approximated. Finally, the analysis was extended to the flow mechanical properties, including the local available binding time, shear rate and rate of elongation obtained from the image-based computational flow modelling. The reported values were averaged over the number of samples at every measurement time. The numbers of samples for different WSRs are $N_{800} = 7$, $N_{1600} = 5$ and $N_{4000} = 3$. The exposure times for WSR = 800 s^{-1} and 1600 s^{-1} are 1, 2, 4, 6, 9, and 12 min. For WSR = 4000 s^{-1} channel occlusion and embolisation events only allowed exposure times of up to 6 min. The total number of processed platelet aggregates is 84. A map of their geometries and platelet density distributions on a flow-parallel cross-section can be found in Fig. 2.

3.1. Aggregate dimensions

The platelet aggregate sizes at different WSR (800–4000 s^{-1}) and exposure times (1–12 min) are presented in Fig. 3. The aggregation size demonstrates a positive correlation with the exposure time across all three WSR values in terms of both aggregation volume and attachment surface area. Notably, the aggregation induced by WSR = 4000 s^{-1} displays persistent growth in terms of aggregation height throughout the entire observation period, whereas the lower WSR cases reach a steady-state in height after 6 min. Furthermore, the aggregates formed for WSR = 4000 s^{-1} exhibit larger dimensions, especially the total aggregation volume and aggregation height, in comparison to results from lower WSRs. These high-shear aggregates demonstrate the fastest, explosive growth, a hallmark of VWF-mediated aggregation [35,54]. Interestingly, the growth rate does not appear to be proportional to the WSR, as shown in Fig. 3A. The lowest, 800 s^{-1} cases display consistently higher growth rates compared to the 1600 s^{-1} cases, potentially due to a difference in shear sensitivity of the various involved binding mechanisms. This hypothesis is detailed further in the *Discussion* section. Similar trends are observable in the aggregate attachment surface

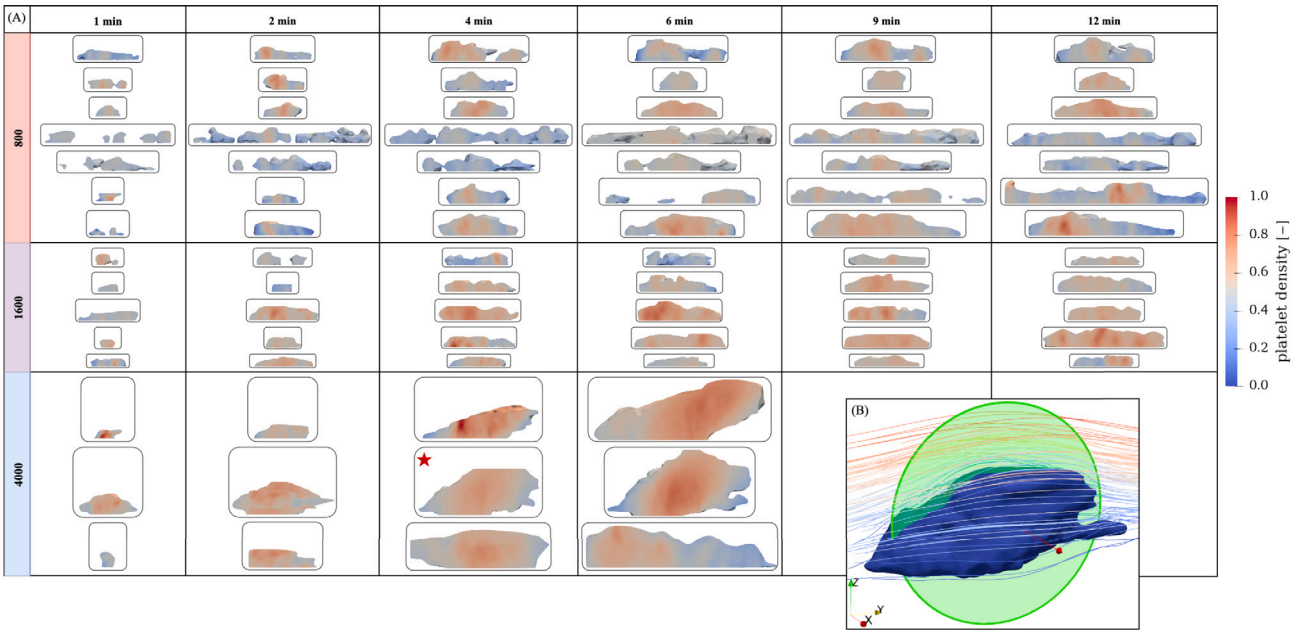

Fig. 2. (A) Platelet density on the cross-section of all 84 platelet aggregates processed in this work. The flow direction is from left to right in all cases. (B) is an illustration showing the cross-section plane used for the aggregate. The lines around the aggregate are the streamlines of blood flow. The chosen aggregate is marked with a red star in (A).

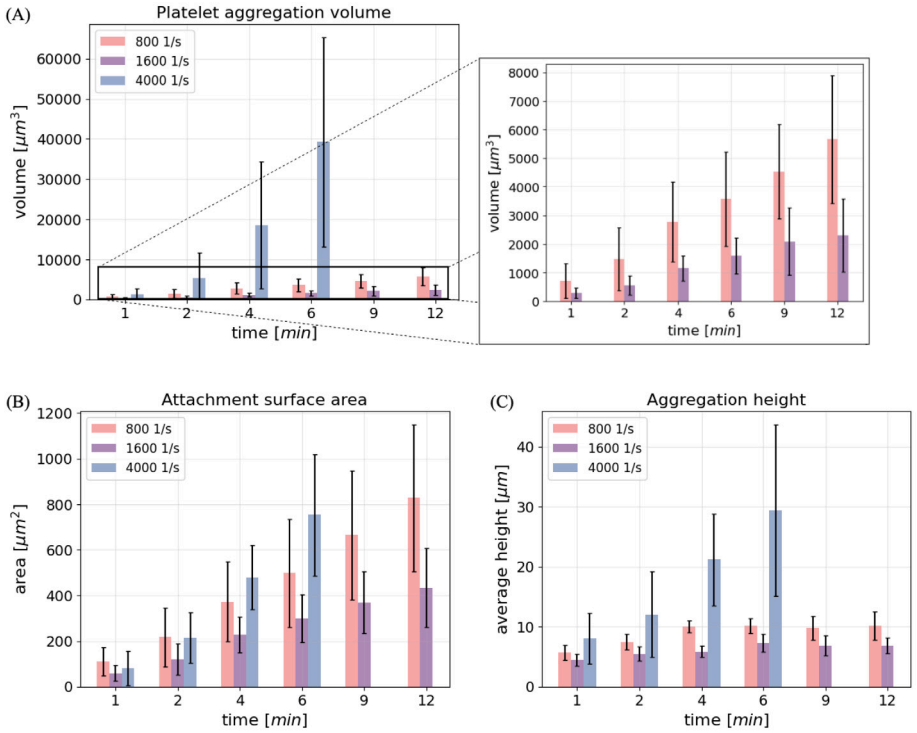

Fig. 3. Size measurements over exposure time: (A) platelet aggregation volume, (B) attachment surface area and (C) aggregation height under different WSRs. The sample numbers for different WSRs are $N_{800} = 7$, $N_{1600} = 5$ and $N_{4000} = 3$. Data are presented as mean ± standard deviation.

area in Fig. 3B. Note that under all WSRs the mean surface area is >200 μm^2 after 4-min exposure, consistently with previous observations [12]. Finally, the two lower WSR conditions show a saturation of the aggregation heights beyond the 4 min mark (Fig. 3C), while the growth continues along the coated channel walls.

3.2. Density distribution of the aggregates

The aggregation process is influenced by the flow conditions, and the growing aggregate, as a porous medium, has a significant impact on the surrounding flow. This feedback loop necessitates the investigation

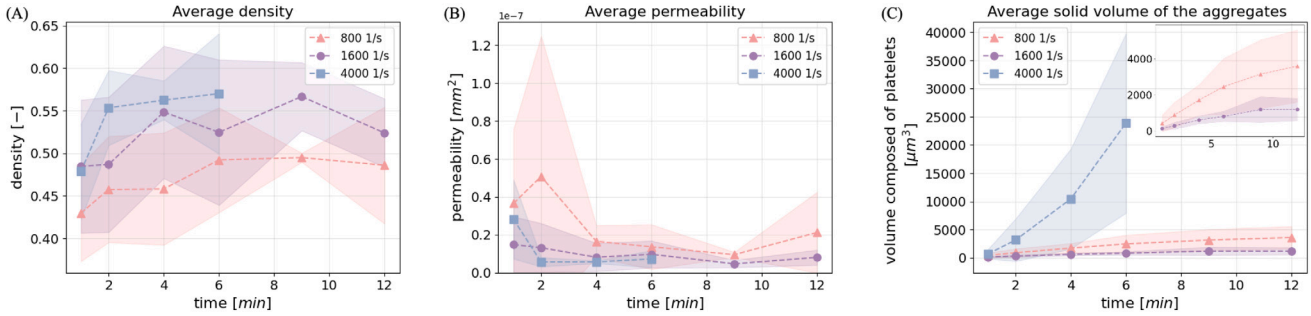

Fig. 4. (A) Average platelet density, (B) average permeability and (C) average solid volume composed of platelets inside the platelet aggregates under different WSR as a function of exposure time. The sample sizes per WSRs are $N_{800} = 7$, $N_{1600} = 5$ and $N_{4000} = 3$. The data is represented as average within these sample groups with st.dev.

of the evolution of the internal structure over time. Fig. 4A and B shows the average measured density and the derived permeability inside the platelet aggregates with different WSRs and exposure duration, respectively. As expected, the aggregates formed under a high WSR exhibit higher internal density distributions compared to those formed under a low WSR, since they need to withstand stronger forces from the flow. Correspondingly, the permeability is higher for aggregates formed under lower WSRs. However, due to the nonlinear relation between permeability and platelet density, there is a sudden increase in the average permeability of aggregates formed under 800 s^{-1} at minute 2 which shows a large standard deviation.

Moreover, the average solid volume quantifies the volume occupied by platelets within aggregates. Fig. 4C presents its changes subjected to different WSRs and exposure times. The behaviour of platelet volume inside these aggregates is analogous to that of the total platelet aggregation volume, showing a positive correlation with exposure time across all three WSR values. The platelet volume inside aggregates formed under WSR = 4000 s^{-1} exhibits consistently explosive growth, while the growth of platelet volume within aggregates induced by lower WSRs is relatively gradual. Notably, similar to total aggregation volume, the growth rate of platelet volume in 800 s^{-1} cases is consistently higher compared to that observed at 1600 s^{-1}.

3.3. Image-based modelling of the fluid mechanics

Based on the 3D shape and density distribution of the aggregates, fluid dynamical simulation was conducted for each of the aggregate samples that matched the boundary flow conditions of the experimental setup. With the help of these simulations detailed characteristics of the flow environment were obtained, including the shear rate and the rate of elongation distribution and the local binding availability time of platelets. Since the pores of the aggregate are too small for platelets to enter [55,56], the aggregation process is restricted to the surface. Therefore, these properties were evaluated along the surface of the platelet aggregates.

Fig. 5A–C shows the local binding availability time, shear rate, and rate of elongation averaged over the surface of the aggregates. The dashed horizontal lines in the figures represent an approximate limiting values associated with characteristic thresholds of the binding processes. Note that these lines are meant as approximate reference points, they correspond to the currently available best estimates in the literature, and represent expected values of wider ranges. For the local binding availability this threshold is in the order of 1 ms, aligning with the binding time required for a weak α IIbβ3-fibrinogen bond characterised by a rupture force within the range of 20–40 pN [16]. VWF-mediated binding is estimated to be at least two orders of magnitudes faster [57], therefore local platelet availability time is not limiting for this process under the investigated flow conditions. However, VWF is a mechanosensitive agent, and in order to be able to capture platelets via GPIbα bonds it needs to undergo conformational change. This can occur as the shear rate reaches the threshold of 2500 s^{-1} or the rate of elongation exceeds 600 s^{-1} in the physiological flow [24]. For the local binding availability time (Fig. 5A), none of the average values on the surface reaches the prescribed threshold. This is due to the presence of small regions with extremely low binding times that are caused by the high velocity spots on the aggregate surfaces. Nevertheless, when comparing this averaged binding availability time across various WSR values, it becomes apparent that the values for the lowest WSR (800 s^{-1}) are the closest to the threshold. In contrast, in the case of both the shear rate (Fig. 5B) and the rate of elongation (Fig. 5C), the average values obtained from the highest WSR (4000 s^{-1}) exhibit close proximity to the prescribed thresholds, with certain cases surpassing these thresholds.

The second row (Fig. 5D–E) shows the ratio of surface areas exceeding these thresholds. For the local binding availability time, platelet aggregates formed under a WSR of 800 s^{-1} have the largest surface area that can facilitate α IIbβ3-fibrinogen binding. It reaches to nearly half of the entire surface. For aggregates formed under 1600 s^{-1}, this ratio ranges from 30% to 40%, while in the case of 4000 s^{-1} WSR, only a very limited portion of the aggregate surface (10%–20%) support low shear rate binding. Conversely, for the thresholds that support GPIbα bonds, the highest area ratio is found on the platelet aggregates formed under high WSR (4000 s^{-1}). Specifically, for both WSR = 800 s^{-1} and 1600 s^{-1} the ratio of the suitable surface area stays small, often less than 10%, throughout the recorded aggregation.

Additionally, the effects of flow direction (and direction of shear and shear gradient) on the growth direction were evaluated. This follows the previous findings [41] that indicate that low shear aggregates tend to grow along the wall, while high shear aggregates grow efficiently perpendicular to the wall. The 3D aggregate shapes were evaluated in separate sections (see the illustration in Fig. 6), as the fluid simulations indicated different characteristic flow behaviour for these regions. Fig. 6A shows that the area with high local binding availability time is predominantly found around the base of the aggregates for all three WSRs. Besides, the values obtained from aggregates formed under WSR = 800 s^{-1} and 1600 s^{-1} are significantly higher compared to those from the highest WSR aggregates.

Fig. 6B and C show that the high shear, and high rate of elongation regions are predominantly located at the top section of the aggregates. For WSR = 800 s^{-1}, these values are close to zero, therefore only results for the other two WSR values are shown. For WSR = 1600 s^{-1} and 4000 s^{-1}, the ratios of both properties above the threshold in the top part of aggregates are significantly higher than those in the bottom section. On the top part, a relatively large surface area of aggregates formed under 4000 s^{-1} is subjected to a high shear rate, while for those aggregates formed under 1600 s^{-1} only less than 20% of the surface area is exposed to such a high shear rate. A similar pattern is visible in terms of elongation rates. Notably, the 1600 s^{-1} WSR cases show a consistent slight decline in both shear rate and rate of elongation ratio during the 12 min of aggregation.

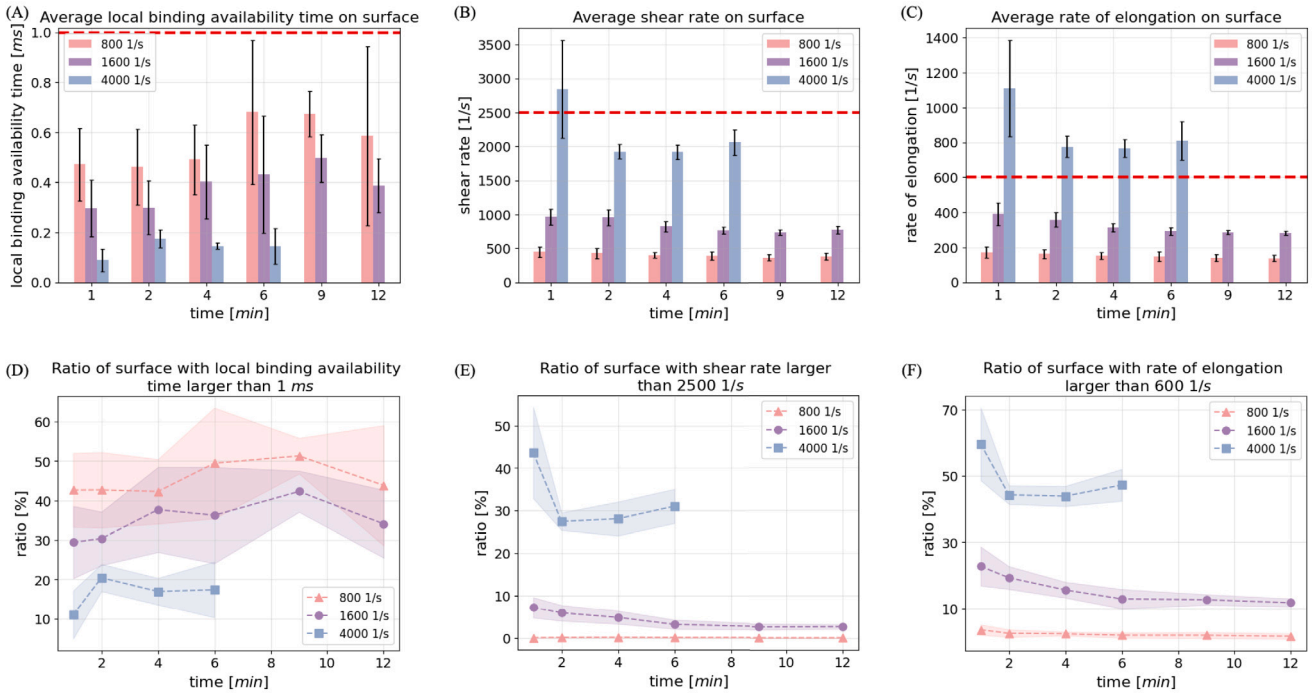

Fig. 5. (A)–(C) Average local binding availability time (A), average shear rate (B) and average rate of elongation (C) at the entire surface of the platelet aggregates. The red dashed line is the threshold for each case. (D)–(E) Ratio of the surface area where local binding availability time (D), shear rate (E) and the rate of elongation (F) are larger than their threshold of platelet aggregates. The sample sizes for different WSRs are $N_{800} = 7$, $N_{1600} = 5$ and $N_{4000} = 3$. Data are presented as mean ± standard deviation.

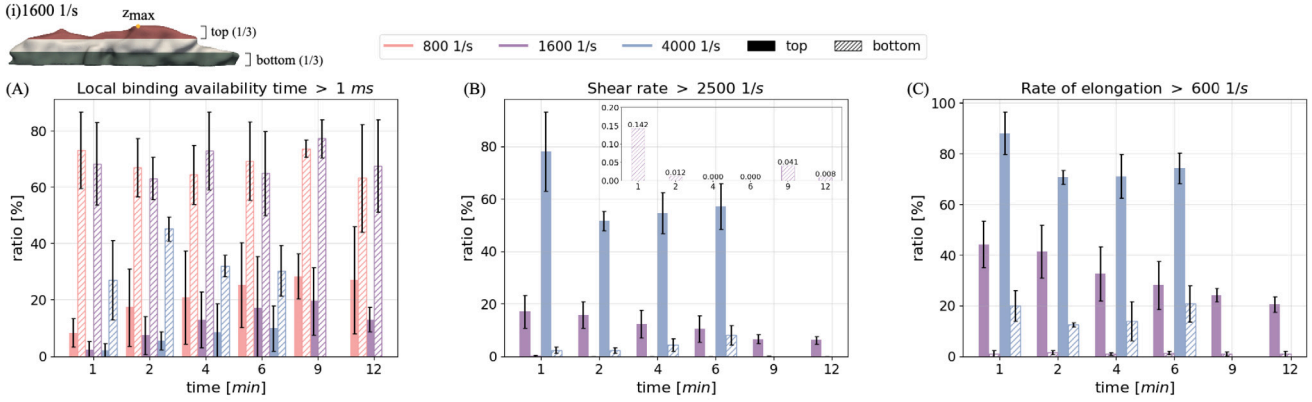

Fig. 6. Ratio of the area where (A) local binding availability time (WSRs = 800, 1600 and 4000 s^{-1}), (B) shear rate (WSRs = 1600 and 4000 s^{-1}) and (C) the rate of elongation (WSRs = 1600 and 4000 s^{-1}) is larger than their threshold at the top part and the bottom part of the platelet aggregates. (i) is an illustration showing the top part and bottom part from the aggregate formed under WSR = 1600 s^{-1}. The small box in (B) is a zoom-in figure showing the ratio of the area where shear rate > 2500 s^{-1} at the bottom part of the aggregates formed under 1600 s^{-1}. The sample sizes for different WSRs are $N_{800} = 7$, $N_{1600} = 5$ and $N_{4000} = 3$. Data are presented as mean ± standard deviation.

4. Discussion

In this study, by leveraging both *in vitro* blood perfusion experiments and computational flow modelling, a detailed study on the platelet aggregation dynamics under different flow conditions were carried out. The aggregation geometries and the internal structure of the aggregates over time were inferred from two modalities of experimental images, containing information on the microstructure. The simulations enable evaluation of flow mechanics associated with platelet aggregates, and enable access to locally varying parameters such as the rate of elongation and shear rate. The local binding availability time, which significantly impacts low shear binding affinity, was also explored using detailed flow information. These properties are currently inaccessible from experiments, however, the combination with *in silico* imaged-based simulation provides an alternative to evaluate them.

The impact of exposure time on the internal density distribution of platelet aggregates formed under three WSRs has been investigated through the analysis of experimental images. In nearly all 84 cases, a high-density core at the central location inside platelet aggregates was found, enveloped by a less dense outer shell (see Fig. 2). This observation aligns with previous research on thrombus structure, however, those results were derived from projections in two dimensions in whole clots [27,29]. To the best of our knowledge, this is the first work to quantitatively assess platelet density within platelet aggregates employing a three-dimensional analysis. Moreover, we found that the aggregates become a bit denser over time (see Fig. 4A). This change is likely influenced by an increase of platelet activation and the dynamics of aggregate retraction [56,58], consequently leading to permeability decrease over time (see Fig. 4B).

Based on the morphology information inferred from the images, the detailed flow environment around the aggregates was computed

at different time points of the exposure. This in turn was used to evaluate the correlation between the properties of the aggregation and the fluid mechanical cues, including shear rate, rate of elongation, and local binding availability time. Higher shear rate and rate of elongation values appeared around the aggregates formed under 4000 s^{-1} WSR compared to those formed under 800 and 1600 s^{-1} WSRs (see Fig. 5). The platelet aggregates formed under high WSR manifest larger dimensions relative to those formed under medium and low WSR (see Fig. 3). In these cases, the average rate of elongation is high enough to activate VWF mediated aggregation pathways that seem to provide a plausible explanation for the explosive growth rate. Moreover, large zones of high shear and rate of elongation are observed at the top part of the platelet aggregates formed under 4000 s^{-1} (see Fig. 6), which is in agreement with preliminary predictions [41]. These flow conditions imply that a considerable portion of the aggregate surface area might be exposed to activated VWF, which in turn facilitates the attachment of platelets to the aggregate surfaces even under high shear. This might be the main driving factor enabling fast channel occlusion in high WSR cases, since these aggregates can efficiently grow upwards into the flow (i.e., perpendicular to the wall). Under low and medium WSRs, the occurrence of a high shear rate and rate of elongation zones is considerably diminished. The top part of the aggregates is still exposed to the highest appearing shear and shear gradients, however, these values are mostly too low to activate VWF. Therefore in these cases the increase in shear only translates to decreasing platelet availability time, and hence to decreased binding probability. This could potentially account for the observation that platelet aggregates formed under these flow conditions nearly cease to grow in height after 4 min, meanwhile their attachment surface area keeps growing steadily (see Fig. 3). It is noteworthy that faster volume growth was observed under 800 s^{-1} compared to 1600 s^{-1} (see Figs. 3 and 4C), which suggests that the aggregation process is a composition of mechanisms that respond differently to shear. For instance, under low shear conditions binding activity is predominantly governed by integrin α IIbβ3 bonds, enabled by long platelet availability times. Under increasing flow the platelet availability time decreases and reduces the probability of a successful binding. At the same time when shear surpasses the necessary shear thresholds the aggregation is increasingly mediated by the high-efficiency VWF to GPIbα binding. Fig. 5A and D indicate that for aggregates formed under 800 s^{-1} the platelet availability (and hence the probability of binding through low shear mechanisms) is consistently higher than for those formed under 1600 s^{-1}. While the shear and shear gradients for both the 800 s^{-1} and 1600 s^{-1} cases remain insufficient for broad VWF activation (see Fig. 5). Therefore the lowest growth rate observed under 1600 s^{-1} WSR implies the existence of a shear range, where the low shear mechanisms are not efficient anymore, while the high shear mechanism have not become fully efficient yet. This in turn means that the crossover in binding efficiency between different binding mechanisms might not be monotonous with the increase of flow, and there might be multiple regions of high and low-efficiency aggregation capability that healthy or pathological processes might exploit. Another possible factor that could contribute to the faster volume growth under 800 s^{-1} compared to 1600 s^{-1} is the detachment of platelets due to the higher flow rate. As demonstrated in [59], the percentage of the detached platelets under 1800 s^{-1} is slightly higher than that under 600 s^{-1}. However, no significant detachments were observed visually during the experiments.

Although this study provides a novel view of the flow environment during platelet aggregation, it is crucial to emphasise assumptions and simplifications. First, the method employed for translating platelet density from fluorescence intensity within aggregates introduced uncertainty, particularly in the case of densely packed platelet aggregates formed under high WSR. However, Hao et al. [41] reported that small variations in platelet density do not yield significant qualitative changes. Moreover, the limited sample size of the experimental dataset for WSR = 4000 s^{-1} resulted in a large standard deviation in the statistical analysis. Performing more experiments could further improve the statistical significance of our findings. In addition, in the computational model of blood flow, the viscosity of blood was assumed to be constant, neglecting the influence of the red blood cell-free layer on blood viscosity. It is also essential to note that VWF uncoiling might require a more extensive region of high shear or shear gradient and the correlation to the size of such zones is not known. The data of the threshold values for VWF conformational change under various conditions is also limited [24]. Furthermore, in this work, we focused on the study of shear rate, rate of elongation and local binding availability time, however, other flow properties such as stress could also influence platelet aggregation. We invite readers to [41] for more details on stress distribution on the surface of the platelet aggregate.

Ultimately, the role of the mechanical signals go beyond the bond formation of platelets. The forces experienced by the platelets, the cues from the flow field, and the stresses in the structure of the aggregate, have pronounced influence on further adhesion, spreading, and activation, and represent triggers for several biochemical pathways [60]. The current work demonstrates the potential in combining 3D imaging data with 3D simulation techniques to access details of the mechanical signals during the aggregation process. This method can be extended to investigate other, more complicated porous structures such as blood clots, and can be further enhanced by including a mechanical simulation to report on the internal stresses of the porous structure. Finally, the results reveal that treatments (such as anti-thrombotic therapies) targeting the biomechanical pathways could benefit from creating conditions that leverage on the low-efficiency zones of aggregation.

5. Conclusion

In this study, we have conducted an in-depth analysis of *in vitro* platelet aggregation experimental images, elucidating the dynamics of platelet aggregation in response to low, medium and high WSRs. The investigation of platelet density distribution inside platelet aggregates demonstrated a consistent region separation across all aggregate samples: a central region characterised by higher platelet density, covered by a less dense shell at the outer layer. Blood flow computational simulations were subsequently performed which enabled the evaluations of the flow mechanical properties such as the local binding availability time, shear rate and rate of elongation on the surfaces of the forming platelet aggregates. Leveraging the data from both experiments and *in silico* simulations, we observed a connection between aggregation direction and flow conditions, where the low shear induces a preference for platelet aggregates to grow parallel to the direction of the blood flow. Furthermore, the correlation of the two binding processes to the platelet aggregation dynamics was investigated. Under low WSR flow conditions, integrin α IIbβ3 mediated binding process is more efficient, while under high WSR, the VWF interaction dominates the binding of platelets. As a result, platelet aggregation at medium WSR levels, which resides in between the high affinity ranges of these two binding mechanisms, exhibits a reduced rate of aggregation and results in relatively smaller aggregates compared to the low and high WSR environments. The observations in this work provide a better understanding of the role of fluid mechanics in the process of platelet aggregation induced by a wide range of shear rates in terms of aggregate morphology and aggregation mechanism.

CRediT authorship contribution statement

Yue Hao: Writing – original draft, Visualization, Software, Methodology, Formal analysis, Conceptualization. **Claudia Tersteeg:** Writing – review & editing, Resources, Investigation. **Alfons G. Hoekstra:** Writing – review & editing, Supervision, Resources, Funding acquisition, Conceptualization. **Gábor Závodszky:** Writing – review & editing, Supervision, Resources, Methodology, Funding acquisition, Conceptualization.

Declaration of competing interest

The authors declare that they have no known competing financial interests or personal relationships that could have appeared to influence the work reported in this paper.

Acknowledgements

This work was supported by the European Union's Horizon Europe research and innovation programme under grant agreement no. 101136438, the GEMINI project (Y.H., G.Z. and A.G.H). The use of supercomputer facilities Snellius (SURF, Netherlands) in this work was sponsored by NWO Exacte Wetenschappen (Physical Sciences).

References

[1] M. Amini, F. Zayeri, M. Salehi, Trend analysis of cardiovascular disease mortality, incidence, and mortality-to-incidence ratio: results from global burden of disease study 2017, BMC Public Health 21 (2021) 401.
[2] F. Violi, D. Pastori, P. Pignatelli, R. Carnevale, Nutrition, thrombosis, and cardiovascular disease, Circ. Res. 126 (2020) 1415–1442.
[3] G. Alkarithi, C. Duval, Y. Shi, F.L. Macrae, R.A. Ariëns, Thrombus structural composition in cardiovascular disease, Arterioscler. Thromb. Vasc. Biol. 41 (2021) 2370–2383.
[4] S.Z. Goldhaber, N. Grasso-Correnti, Treatment of blood clots, Circulation 106 (2002) e138–e140.
[5] J. Papp, P. Kenyeres, K. Toth, Clinical importance of antiplatelet drugs in cardiovascular diseases, Clin. Hemorheol. Microcirc. 53 (2013) 81–96, 1-2.
[6] A. Rana, E. Westein, B. Niego, C.E. Hagemeyer, Shear-dependent platelet aggregation: Mechanisms and therapeutic opportunities, Front. Cardiovascul. Med. 6 (2019).
[7] T.T. Tsai, P.M. Ho, S. Xu, J.D. Powers, N.M. Carroll, S.M. Shetterly, T.M. Maddox, J.S. Rumsfeld, K. Margolis, A.S. Go, D.J. Magid, Increased risk of bleeding in patients on clopidogrel therapy after drug-eluting stents implantation, Circ.: Cardiovasc. Interv. 3 (2010) 230–235.
[8] Z.M. Ruggeri, J.N. Orje, R. Habermann, A.B. Federici, A.J. Reininger, Activation-independent platelet adhesion and aggregation under elevated shear stress, Blood 108 (2006) 1903–1910.
[9] B.J.M. van Rooij, G. Závodszky, A.G. Hoekstra, D.N. Ku, Biorheology of occlusive thrombi formation under high shear: in vitro growth and shrinkage, Sci. Rep. 10 (2020) 18604.
[10] D.A. Kim, D.N. Ku, Structure of shear-induced platelet aggregated clot formed in an in vitro arterial thrombosis model, Blood Adv. 6 (2022) 2872–2883.
[11] K.G. Link, M.G. Sorrells, N.A. Danes, K.B. Neeves, K. Leiderman, A.L. Fogelson, A mathematical model of platelet aggregation in an extravascular injury under flow, Multiscale Model. Simul. 18 (2020) 1489–1524.
[12] C.H.H. Chan, M. Inoue, K.K. Ki, T. Murashige, J.F. Fraser, M.J. Simmonds, G.D. Tansley, N. Watanabe, Shear-dependent platelet aggregation size, Artif. Organs. 44 (2020) 1286–1295.
[13] R.I. Litvinov, D.H. Farrell, J.W. Weisel, J.S. Bennett, The platelet integrin αiibβ3 differentially interacts with fibrin versus fibrinogen*, J. Biol. Chem. 291 (2016) 7858–7867.
[14] P. Gupta, P. Zhang, J. Sheriff, D. Bluestein, Y. Deng, A multiscale model for multiple platelet aggregation in shear flow, Biomech. Model. Mechanobiol. 20 (2021) 1013–1030.
[15] W.S. Nesbitt, E. Westein, F.J. Tovar-Lopez, E. Tolouei, A. Mitchell, J. Fu, J. Carberry, A. Fouras, S.P. Jackson, A shear gradient–dependent platelet aggregation mechanism drives thrombus formation, Nat. Med. 15 (2009) 665–673.
[16] R.I. Litvinov, J.S. Bennett, J.W. Weisel, H. Shuman, Multi-step fibrinogen binding to the integrin α iibβ3 detected using force spectroscopy, Biophys. J. 89 (2005) 2824–2834.
[17] Z.M. Ruggeri, The role of von willebrand factor in thrombus formation, Thromb. Res. 120 (2007) S5–S9, Von Willebrand: The Scientist, The Disease, The Factor and The Treatment.
[18] S. Gogia, S. Neelamegham, Role of fluid shear stress in regulating vwf structure, function and related blood disorders, Biorheology 52 (2015) 319–335, 5-6.
[19] S. Kania, A. Oztekin, X. Cheng, X.F. Zhang, E. Webb, Predicting pathological von willebrand factor unraveling in elongational flow, Biophys. J. 120 (2021) 1903–1915.
[20] E. Di Stasio, R. De Cristofaro, The effect of shear stress on protein conformation: Physical forces operating on biochemical systems: The case of von willebrand factor, Biophys. Chem. 153 (2010) 1–8.
[21] T.A. Springer, Von willebrand factor, jedi knight of the bloodstream, Blood 124 (2014) 1412–1425.
[22] S.W. Schneider, S. Nuschele, A. Wixforth, C. Gorzelanny, A. Alexander-Katz, R.R. Netz, M.F. Schneider, Shear-induced unfolding triggers adhesion of von willebrand factor fibers, Proc. Natl. Acad. Sci. 104 (2007) 7899–7903.
[23] S. Lippok, M. Radtke, T. Obser, L. Kleemeier, R. Schneppenheim, U. Budde, R.R. Netz, J.O. Rädler, Shear-induced unfolding and enzymatic cleavage of full-length vwf multimers, Biophys. J. 110 (2016) 545–554.
[24] C.E. Sing, A. Alexander-Katz, Elongational flow induces the unfolding of von willebrand factor at physiological flow rates, Biophys. J. 98 (2010) L35–L37.
[25] I. Singh, E. Themistou, L. Porcar, S. Neelamegham, Fluid shear induces conformation change in human blood protein von willebrand factor in solution, Biophys. J. 96 (2009) 2313–2320.
[26] R.S. Voronov, T.J. Stalker, L.F. Brass, S.L. Diamond, Simulation of intrathrombus fluid and solute transport using in vivo clot structures with single platelet resolution, Ann. Biomed. Eng. 41 (2013) 1297–1307.
[27] T.J. Stalker, E.A. Traxler, J. Wu, K.M. Wannemacher, S.L. Cermignano, R. Voronov, S.L. Diamond, L.F. Brass, Hierarchical organization in the hemostatic response and its relationship to the platelet-signaling network, Blood 121 (2013) 1875–1885.
[28] A. Wufsus, N. Macera, K. Neeves, The hydraulic permeability of blood clots as a function of fibrin and platelet density, Biophys. J. 104 (2013) 1812–1823.
[29] J.D. Welsh, T.J. Stalker, R. Voronov, R.W. Muthard, M. Tomaiuolo, S.L. Diamond, L.F. Brass, A systems approach to hemostasis: 1. The interdependence of thrombus architecture and agonist movements in the gaps between platelets, Blood 124 (2014) 1808–1815.
[30] J. Du, D. Kim, G. Alhawael, D.N. Ku, A.L. Fogelson, Clot permeability, agonist transport, and platelet binding kinetics in arterial thrombosis, Biophys. J. 119 (2020) 2102–2115.
[31] R.W. Muthard, S.L. Diamond, Blood clots are rapidly assembled hemodynamic sensors, Arterioscler. Thromb. Vasc. Biol. 32 (2012) 2938–2945.
[32] C.L. Slaboch, M.S. Alber, E.D. Rosen, T.C. Ovaert, Mechano-rheological properties of the murine thrombus determined via nanoindentation and finite element modeling, J. Mech. Behav. Biomed. Mater. 10 (2012) 75–86.
[33] K. Leiderman, A.L. Fogelson, The influence of hindered transport on the development of platelet thrombi under flow, Bull. Math. Biol. 75 (2013) 1255–1283.
[34] C. Ldc, G. Se, Relative contributions of von Willebrand factor and platelets in high shear thrombosis, J. Hematol. Thromboembolic Dis. 4 (2016) 1–8.
[35] L.D. Casa, D.N. Ku, Thrombus formation at high shear rates, Annu. Rev. Biomed. Eng. 19 (2017) 415–433, PMID: 28441034.
[36] B.J.M. van Rooij, G. Závodszky, A.G. Hoekstra, D.N. Ku, Haemodynamic flow conditions at the initiation of high-shear platelet aggregation: a combined in *vitro* and cellular *in silico* study, Interface Focus 11 (2021) 20190126.
[37] Z.L. Liu, D.N. Ku, C.K. Aidun, Mechanobiology of shear-induced platelet aggregation leading to occlusive arterial thrombosis: A multiscale in silico analysis, J. Biomech. 120 (2021) 110349.
[38] A. Yazdani, H. Li, J.D. Humphrey, G.E. Karniadakis, A general shear-dependent model for thrombus formation, PLoS Comput. Biol. 13 (2017) 1–24.
[39] K.N. Shankar, Y. Zhang, T. Sinno, S.L. Diamond, A three-dimensional multiscale model for the prediction of thrombus growth under flow with single-platelet resolution, PLoS Comput. Biol. 18 (2022) 1–19.
[40] M. Zhussupbekov, R. Méndez Rojano, W.-T. Wu, J.F. Antaki, Von willebrand factor unfolding mediates platelet deposition in a model of high-shear thrombosis, Biophys. J. 121 (2022) 4033–4047.
[41] Y. Hao, G. Závodszky, C. Tersteeg, M. Barzegari, A.G. Hoekstra, Image-based flow simulation of platelet aggregates under different shear rates, PLoS Comput. Biol. 19 (2023) 1–20.
[42] A. Fedorov, R. Beichel, J. Kalpathy-Cramer, J. Finet, J.-C. Fillion-Robin, S. Pujol, C. Bauer, D. Jennings, F. Fennessy, M. Sonka, J. Buatti, S. Aylward, J.V. Miller, S. Pieper, R. Kikinis, 3D slicer as an image computing platform for the quantitative imaging network, Magn. Reson. Imaging 30 (2012) 1323–1341, Quantitative Imaging in Cancer.
[43] C. Geuzaine, J.-F. Remacle, Gmsh: A 3-d finite element mesh generator with built-in pre- and post-processing facilities, Internat. J. Numer. Methods Engrg. 79 (2009) 1309–1331.
[44] R. Courant, K. Friedrichs, H. Lewy, On the partial difference equations of mathematical physics, IBM J. Res. Dev. 11 (1967) 215–234.
[45] R.J. Trudnowski, R.C. Rico, Specific Gravity of Blood and Plasma at 4 and 37 °C, Clin. Chem. 20 (1974) 615–616.
[46] E.W. Merrill, G.A. Pelletier, Viscosity of human blood: transition from newtonian to non-newtonian, J. Appl. Physiol. 23 (1967) 178–182, PMID: 6040532.
[47] S. Lee, S. Jang, Y. Park, Measuring three-dimensional dynamics of platelet activation using 3-d quantitative phase imaging, 2019, bioRxiv.
[48] P. Bath, R. Butterworth, Platelet size: measurement, physiology and vascular disease, Blood Coagul. Fibrinolysis 7 (1996) 157—161.
[49] F. Hecht, New development in freefem++, J. Numer. Math. 20 (2012) 251–265.
[50] S.R. Simmons, P.A. Sims, R.M. Albrecht, α Iibβ3 redistribution triggered by receptor cross-linking, Arterioscler. Thromb. Vasc. Biol. 17 (1997) 3311–3320.
[51] C.J. Petrie, Extensional viscosity: A critical discussion, J. Non-Newton. Fluid Mech. 137 (2006) 15–23, Extensional Flow.
[52] C.J. Spieker, G. Závodszky, C. Mouriaux, M. van der Kolk, C. Gachet, P.H. Mangin, A.G. Hoekstra, The effects of micro-vessel curvature induced elongational flows on platelet adhesion, Ann. Biomed. Eng. 49 (2021) 3609–3620.

[53] C.J. Spieker, G. Závodszky, C. Mouriaux, P.H. Mangin, A.G. Hoekstra, Initial platelet aggregation in the complex shear environment of a punctured vessel model, Phys. Fluids 35 (2023) 071904.
[54] L.D. Casa, D.H. Deaton, D.N. Ku, Role of high shear rate in thrombosis, J. Vasc. Surg. 61 (2015) 1068–1080.
[55] M. Tomaiuolo, T.J. Stalker, J.D. Welsh, S.L. Diamond, T. Sinno, L.F. Brass, A systems approach to hemostasis: 2. Computational analysis of molecular transport in the thrombus microenvironment, Blood 124 (2014) 1816–1823.
[56] M. Mirramezani, B.A. Herbig, T.J. Stalker, L. Nettey, M. Cooper, J.W. Weisel, S.L. Diamond, T. Sinno, L.F. Brass, S.C. Shadden, M. Tomaiuolo, Platelet packing density is an independent regulator of the hemostatic response to injury, J. Thromb. Haemost. 16 (2018) 973–983.
[57] Z.L. Liu, C. Bresette, C.K. Aidun, D.N. Ku, SIPA in 10 milliseconds: VWF tentacles agglomerate and capture platelets under high shear, Blood Adv. 6 (2022) 2453–2465.
[58] D. Gao, C.W. Sun, A.B. Woodley, J.-f. Dong, Clot retraction and its correlation with the function of platelet integrin αiibβ3, Biomedicines 11 (2023).
[59] S. Kulkarni, S.M. Dopheide, C.L. Yap, C. Ravanat, M. Freund, P. Mangin, K.A. Heel, A. Street, I.S. Harper, F. Lanza, S.P. Jackson, A revised model of platelet aggregation, J. Clin. Invest. 105 (2000) 783–791.
[60] Y. Qiu, A.C. Brown, D.R. Myers, Y. Sakurai, R.G. Mannino, R. Tran, B. Ahn, E.T. Hardy, M.F. Kee, S. Kumar, G. Bao, T.H. Barker, W.A. Lam, Platelet mechanosensing of substrate stiffness during clot formation mediates adhesion, spreading, and activation, Proc. Natl. Acad. Sci. 111 (2014) 14430–14435.